

Anisotropic superconductivity in topological crystalline metal $\text{Pb}_{1/3}\text{TaS}_2$ with multiple Dirac fermions

Xiaohui Yang,^{1,2,*} Tonghua Yu,^{3,†} Chenchao Xu,³ Jialu Wang,^{1,2} Wanghua Hu,^{1,2} Zhuokai Xu,^{1,2} Tao Wang,^{1,2} Chao Zhang,⁴ Zhi Ren,^{1,2} Zhu-an Xu,^{5,6} Motoaki Hirayama,^{3,7} Ryotaro Arita,^{3,7} and Xiao Lin^{1,2,‡}

¹*Institute of Natural Sciences, Westlake Institute for Advanced Study, Hangzhou 310024, P. R. China*

²*Key Laboratory for Quantum Materials of Zhejiang Province,*

School of Science, Westlake University, Hangzhou 310024, P. R. China

³*Department of Applied Physics, University of Tokyo, Tokyo 113-8656, Japan*

⁴*Instrumentation and Service Center for Physical Sciences, Westlake University, Hangzhou 310024, China*

⁵*Zhejiang Province Key Laboratory of Quantum Technology and Device,*

Department of Physics, Zhejiang University, Hangzhou 310027, P. R. China

⁶*State Key Lab of Silicon Materials, Zhejiang University, Hangzhou 310027, P. R. China*

⁷*RIKEN Center for Emergent Matter Science, 2-1 Hirosawa, Wako, 351-0198, Japan*

(Dated: January 8, 2022)

Topological crystalline metals/semimetals (TCMs) have stimulated a great research interest, which broaden the classification of topological phases and provide a valuable platform to explore topological superconductivity. Here, we report the discovery of superconductivity and topological features in Pb-intercalated transition-metal dichalcogenide $\text{Pb}_{1/3}\text{TaS}_2$. Systematic measurements indicate that $\text{Pb}_{1/3}\text{TaS}_2$ is a quasi-two-dimensional (q-2D) type-II superconductor ($T_c \approx 2.8$ K) with a significantly enhanced anisotropy of upper critical field ($\gamma_{H_{c2}} = H_{c2}^{ab}/H_{c2}^c \approx 17$). In addition, first-principles calculations reveal that $\text{Pb}_{1/3}\text{TaS}_2$ hosts multiple topological Dirac fermions in the electronic band structure. We discover four groups of Dirac nodal lines on the $k_z = \pi$ plane and two sets of Dirac points on the rotation/screw axes, which are protected by crystalline symmetries and robust against spin-orbit coupling (SOC). Dirac-cone-like surface states emerge on the (001) surface because of band inversion. Our work shows that the TCM candidate $\text{Pb}_{1/3}\text{TaS}_2$ is a promising arena to study the interplay between superconductivity and topological Dirac fermions.

Introduction

The search for exotic topological phases of condensed matter has attracted a significant attention since the discovery of topological insulators (TIs), a unique class of electronic systems that show insulating bulks and topologically protected boundary excitations^{1–9}. Shortly following TIs, topological metals/semimetals (TSMs) with bulk band crossings close to the Fermi level are broadly proposed and verified^{10–18}. Because of the topological bulk and surface states, for instance, nodal-line metals/semimetals (NLSMs) exhibit unconventional transport features, such as three-dimensional quantum Hall effect (3D QHE) and high-temperature surface superconductivity^{19,20}. In the absence of magnetism, a centrosymmetric TSM, where both spatial inversion (\mathcal{P}) and time reversal (\mathcal{T}) symmetries are preserved, may host quadruply degenerate bulk nodes resembling massless Dirac fermions^{11,13}. Compared with the noncentrosymmetric case, however, these degeneracies are unstable under significant spin-orbit coupling (SOC) unless extra crystalline symmetries are present¹⁰. To be more specific, apart from the \mathcal{PT} protection, a stable Dirac nodal point entails the guarantee of a rotation or screw symmetry^{11,13}, and a Dirac nodal line can be supported by additional nonsymmorphic operations^{21–24}. Crystalline symmetries are therefore an essential factor for the search of TSMs hosting stable bulk Dirac fermions. We alternatively refer to such TSMs as topological crystalline metals/semimetals (TCMs)²⁵.

Recently, the family of the so-called 112 systems, MTX_2 ($M = \text{Pb, Sn, Tl or In}$, $T = \text{Ta or Nb}$, $X = \text{Se or S}$), have created a surge of research activities, because of the superconductivity and rich topological nature^{26–30}. The noncentrosymmetric PbTaSe_2 (derived from $1H\text{-TaSe}_2$ by intercalating Pb in the van der Waals gap) was reported to be a promising topological superconductor (TSC) candidate, due to the observation of zero-energy Majorana bound states in the vortices³¹. PbTaSe_2 is also a typical NLSM where the nodal lines are guaranteed by mirror symmetry⁸. A different group of 112 systems with centrosymmetric lattices, e.g., PbTaS_2 ³² and SnTaS_2 ³³, in which the nodal lines are protected by the \mathcal{PT} symmetry instead, without the account of SOC. Nevertheless, nodal lines in the centrosymmetric 112 systems receive no nonsymmorphic protection and thus cannot survive under the strong SOC³³.

Herein, based on symmetry analysis and band calculations, we predict a new TCM candidate, the centrosymmetric crystal $\text{Pb}_{1/3}\text{TaS}_2$ that hosts multiple stable nodal point and line structures. In contrast to the above-mentioned 112 systems, nodal lines in $\text{Pb}_{1/3}\text{TaS}_2$ are robust against SOC by virtue of the nonsymmorphic symmetry. Dirac points are furthermore unveiled, stabilized by rotation/screw symmetries. Band inversion gives rise to Dirac-cone-like surface states in the (001) surface.

* Equal contributions; yangxiaohui@westlake.edu.cn

† Equal contributions

‡ linxiao@westlake.edu.cn

In addition, we synthesize and characterize this single crystal in experiment. The results show that $\text{Pb}_{1/3}\text{TaS}_2$ peculiarly exhibits quasi-two-dimensional (q-2D) superconductivity ($T_c = 2.8$ K) with large anisotropy in upper critical field H_{c2} . Consequently, the superconductor $\text{Pb}_{1/3}\text{TaS}_2$ is a unique electronic system manifesting versatile nontrivial topological nature, offering a realistic material testbed for the exploration of the Dirac fermions and even possible TSC.

Results

Sample characterizations $\text{Pb}_{1/3}\text{TaS}_2$ is centrosymmetric with a hexagonal structure and a space group $P6_3/mcm$ (No. 193)³⁴. As illustrated in Fig. 1(a), Ta atoms are in trigonal-prismatic coordination by S atoms and the stacking sequence of S-Ta-S sandwiches follows that in $2H\text{-TaS}_2$ ³⁵. Pb atoms are intercalated in between TaS_2 layers, but the occupation number is only one third of that in 112 PbTaS_2 phase³². Fig. 1(b) presents the XRD pattern of $\text{Pb}_{1/3}\text{TaS}_2$ single crystals normal to ab-plane. The inset shows the full width at half-maximum (FWHM) of the (0010) peak is only 0.04° , indicating the high crystalline quality. The interplanar spacing is calculated to be 14.84 Å by employing the least-square method. According to the EDX data (see Fig. S1 of Supporting Information), the molar-ratio between Pb, Ta and S atoms amounts to 1: 3: 6, in good agreement with the nominal one.

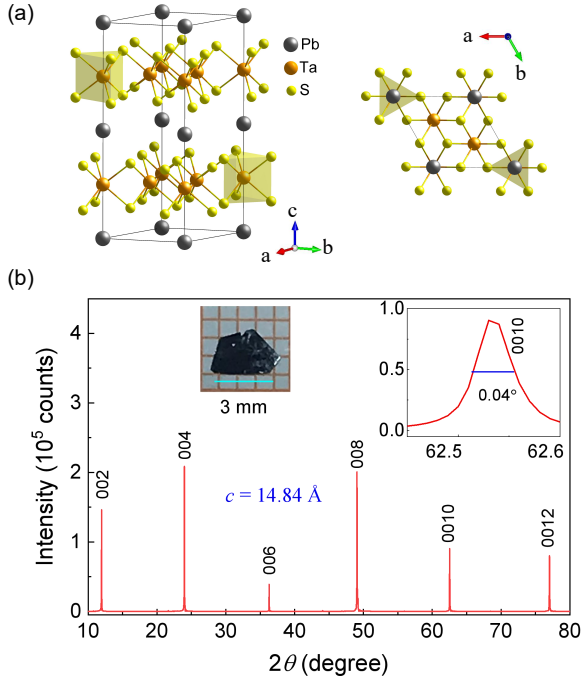


FIG. 1. (a) The crystal structure of $\text{Pb}_{1/3}\text{TaS}_2$ along different directions. (b) XRD pattern of the single crystal with (00l) reflections, the inset of the right panel zooms in the (0010) reflection.

Fig. 2(a) shows the in-plane resistivity ρ_{ab} as a function of temperature T for $\text{Pb}_{1/3}\text{TaS}_2$, which exhibits metallic behavior with a high residual resistivity ratio ($RRR = \rho(300\text{K})/\rho(3\text{K})$) amounting to 24. The zoom-in figure in the inset of Fig. 2(a) shows a sharp superconducting transition, $T_c^{50\%}$ of which determined at the half value of the normal state resistivity is around 2.8 K, higher than $2H\text{-TaS}_2$ ($T_c = 0.8$ K)³⁶ and PbTaS_2 ($T_c = 2.6$ K)³². Fig. 2(b) shows the T dependence of dc magnetic susceptibility with an external magnetic field ($H = 2$ Oe) along ab-plane. The diamagnetic signal reveals a superconducting transition at 2.7 K in consistent with transport measurements. The shielding volume fraction of superconductivity is close to 100% from the zero-field cooling (ZFC) process.

The Hall data ρ_{yx} at different temperatures is presented in Fig. 2(c). ρ_{yx} is positive and linear in field, which suggests holes dominate in charge transport. The inset of Fig. 2(c) presents the Hall coefficient $R_H = \rho_{yx}/H$, which varies slowly with T . Note that the carrier concentration n cannot be directly deduced from R_H given the multi-band nature of $\text{Pb}_{1/3}\text{TaS}_2$ (see the band structure below).

Fig. 2(d)-(e) show the T dependent ρ_{ab} at various fields perpendicular and parallel to the ab-plane, respectively. The superconducting transition broadens and shifts towards lower temperatures by increasing fields, due to a field-induced pair breaking effect. The upper critical field for $H//ab$ (H_{c2}^{ab}) and $H//c$ (H_{c2}^c) versus $T_c^{50\%}$ are summarized in Fig. 2(f), which exhibits an upward curvature. Similar features were reported in PbTaSe_2 ³⁷ and PbTaS_2 ³², in which the upward feature was roughly fitted by

$$H_{c2}(t) = H_{c2}(0)(1 - t^{3/2})^{3/2} \quad (1)$$

where $t = T/T_c$. Eq. 1 arises from a local-pairing mechanism³⁸. However, Eq. 1 does not fit our data well.

An alternative interpretation of the upward feature suggests that $\text{Pb}_{1/3}\text{TaS}_2$ has multi-gap nature, as in MgB_2 ^{39,40}, NbSe_2 ⁴¹ and some iron-based superconductors⁴²⁻⁴⁴. As seen in Fig. 2(f), the data is well fitted by a two-gap model⁴⁵:

$$a_0[\ln t + U(h)][\ln t + U(\eta h)] + a_1[\ln t + U(h)] + a_2[\ln t + U(\eta h)] = 0 \quad (2)$$

where $t = T/T_c$ and $h = H_{c2}D_1/(2\phi_0/T)$ is the reduced temperature and critical field, in which $a_0 = 2(\lambda_{11}\lambda_{22} - \lambda_{12}\lambda_{21})$, $a_1 = 1 + (\lambda_{11} - \lambda_{22})/\lambda_0$, $a_2 = 1 - (\lambda_{11} - \lambda_{22})/\lambda_0$, $\lambda_0 = ((\lambda_{11} - \lambda_{22})^2 + 4\lambda_{12}\lambda_{21})^{1/2}$, $\eta = D_2/D_1$ and $U(x) = \psi(1/2 + x) - \psi(1/2)$. λ_{11} (λ_{22}) and λ_{12} (λ_{21}) are the intraband and interband BCS coupling constants, respectively, $\psi(x)$ is the digamma function, D_1 and D_2 are the diffusivity of each band.

According to the fitting, the upper critical field at zero- T $H_{c2}^{ab}(0)$ and $H_{c2}^c(0)$ are estimated to be 6.84 T

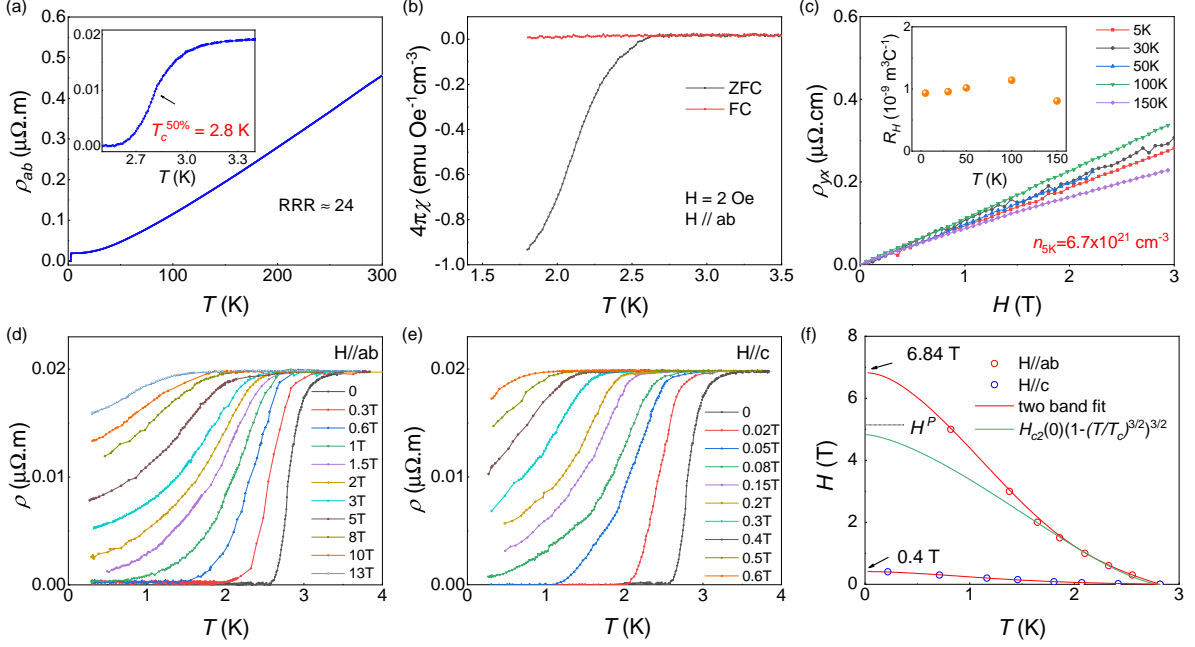


FIG. 2. (a) T dependence of the electrical resistivity ρ_{ab} of $\text{Pb}_{1/3}\text{TaS}_2$ single crystal. The inset shows the superconducting transition around T_c . (b) T dependence of dc magnetic susceptibility ($H//ab$, $H = 2$ Oe) around T_c . (c) Magnetic field dependence of Hall resistivity for $\text{Pb}_{1/3}\text{TaS}_2$ at different temperatures. Inset: the Hall coefficient vs. temperature. (d) and (e) The low T resistivity under different magnetic fields of single crystal, magnetic field parallel and perpendicular to the ab -plane, respectively. (f) T dependence of the H_{c2} with two-band fits for both directions, the black line dictates the Pauli paramagnetic limit.

and 0.4 T, respectively. The in-plane $H_{c2}^{ab}(0)$ slightly exceeds the Pauli paramagnetic limit ($\mu_0 H_P^{BCS}(0) = 1.84 T_c \approx 5.15$ T). Subsequently, the superconducting coherence length is calculated to be $\xi_{ab}(0) \approx 28.7$ nm and $\xi_c(0) \approx 1.68$ nm through the Ginzburg-Landau (GL) formula: $H_{c2}^c = \Phi_0/2\pi\xi_{ab}^2$ and $H_{c2}^c = \Phi_0/2\pi\xi_{ab}\xi_c$. Interestingly, $\xi_c(0)$ is close to the lattice constant. Moreover, the superconducting anisotropy ($\gamma_{H_{c2}} = H_{c2}^{ab}/H_{c2}^c$) is as large as 17.1, larger than that in $2H\text{-TaS}_2$ (6.7)⁴⁶, which is consistent with the fact that the distance between adjacent TaS_2 blocks is 7.42 Å for $\text{Pb}_{1/3}\text{TaS}_2$, larger than 6.05 Å of $2H\text{-TaS}_2$ ⁴⁷. Above all, the results indicate the q-2D superconducting nature in $\text{Pb}_{1/3}\text{TaS}_2$.

In order to gain further information of the superconducting state, the isothermal magnetization $M(H)$ with field along ab -plane is presented in Fig. 3(a) at various temperatures. The inset shows the full magnetization loop at 1.8 K, indicating $\text{Pb}_{1/3}\text{TaS}_2$ is a typical type-II superconductor.

The in-plane lower critical field H_{c1}^{ab} can be determined at the point which the magnetization curve starts to deviate from the linear Meissner response. H_{c1}^{ab} versus T is plotted in Fig. 3(b), which is fitted by the conventional formula $H_{c1}(T) = H_{c1}(0)[1 - (T/T_c)^2]$ for a weakly coupled superconductor⁴⁸. H_{c1}^{ab} at zero- T is estimated to be 16.3 Oe.

Using the relationship $H_{c2}^{ab}(0)/H_{c1}^{ab}(0) = 2\kappa_{ab}^2/\ln\kappa_{ab}$ and $\kappa_{ab}(0) = \lambda_{ab}(0)/\xi_c(0)$, we estimate the GL param-

eter $\kappa_{ab} \sim 98.1$ and penetration depth $\lambda_{ab}(0) \sim 164.8$ nm, the resulted parameters are summarized in Table I for brevity, indicating $\text{Pb}_{1/3}\text{TaS}_2$ is an extreme type-II superconductor with highly anisotropic properties.

TABLE I. The anisotropic superconducting parameters of $\text{Pb}_{1/3}\text{TaS}_2$ single crystal.

Parameters	Values (unit)
$H_{c2}^{ab}(0)$	6.84 (T)
$H_{c2}^c(0)$	0.4 (T)
$\xi_{ab}(0)$	28.7 (nm)
$\xi_c(0)$	1.68 (nm)
$H_{c1}^{ab}(0)$	16.3 (Oe)
$\lambda_{ab}(0)$	164.8 (nm)
κ_{ab}	98.1
$\gamma_{H_{c2}}$	17.1

Band structures Now we report the topological electronic bands of the $\text{Pb}_{1/3}\text{TaS}_2$ system predicted by our first-principles calculations. Fig. 4(a) presents the electronic band structure of $\text{Pb}_{1/3}\text{TaS}_2$ in the presence of SOC, with high-symmetry k points given in Fig. 4(b). Six isolated bands (numbered as band 1 to 6 from low to high energy) are located in the vicinity of the Fermi energy. Each band has double degeneracy (Kramers pair) because of the \mathcal{PT} symmetry. The band dispersion along the k_z direction (i.e., $A\text{-}\Gamma$, $K\text{-}H$) is relatively weak in

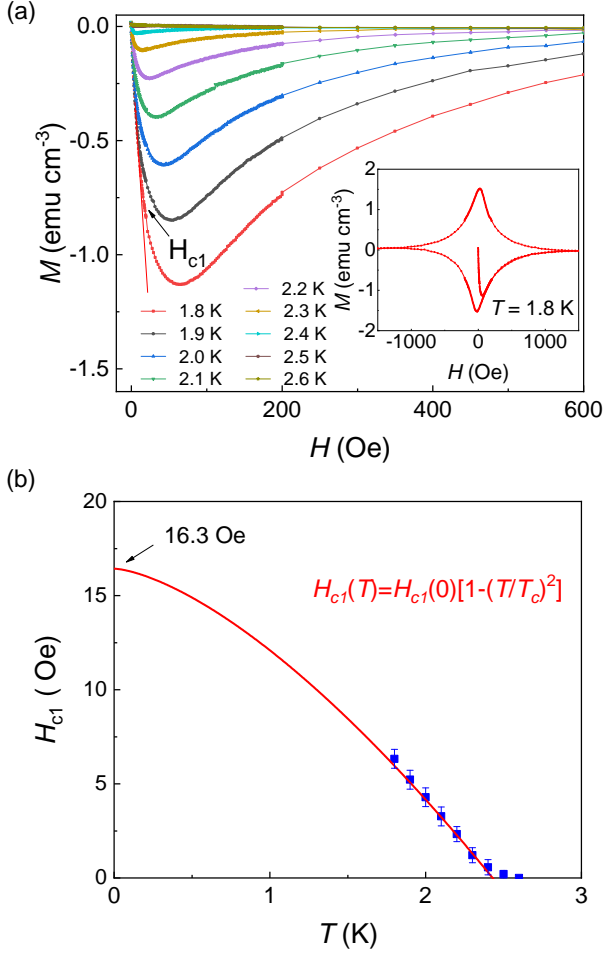


FIG. 3. (a) Magnetization $M(H)$ curves at various temperatures of $\text{Pb}_{1/3}\text{TaS}_2$ single crystal, the inset shows the loop taken at 1.8 K. (b) The superconducting H - T phase diagram of $\text{Pb}_{1/3}\text{TaS}_2$.

comparison to that along the in-plane direction (i.e., A - L - H - A , Γ - M - K), indicating the q-2D of the material, in agreement with the experimental observation.

For further analysis, it is essential to list the crystalline symmetries in $\text{Pb}_{1/3}\text{TaS}_2$ that are of particular importance: three vertical mirrors $\mathcal{M}_{[1\bar{1}0]} = \{\bar{2}[1\bar{1}0] | 0, 0, 0\}$, $\mathcal{M}_{[120]} = \{\bar{2}[120] | 0, 0, 0\}$, $\mathcal{M}_{[210]} = \{\bar{2}[210] | 0, 0, 0\}$, a horizontal mirror $\mathcal{M}_{[001]} = \{\bar{2}[001] | 0, 0, \frac{1}{2}\}$, a threefold rotation $\mathcal{C}_{3[001]} = \{3[001] | 0, 0, 0\}$, and a sixfold screw $\tilde{\mathcal{C}}_{6[001]} = \{6[001] | 0, 0, \frac{1}{2}\}$. In combination with vertical mirrors and the \mathcal{PT} symmetry, $\mathcal{M}_{[001]}$ nonsymmorphically dictates multiple Dirac nodal lines on the $k_z = \pi$ plane [colored by blue in Fig. 4(b)] for every two bands^{23,24}. We refer to the nodal lines between bands 1 and 2 as NL1, similarly for NL2 and NL3, as illustrated in Fig. 4(a). Crossing bands for each nodal line are distinguished by opposite $\mathcal{M}_{[001]}$ eigenvalues (i or $-i$) as shown in Fig. 4(a). Detailed argument can be found in Supporting Information. Apart from the symmetry-enforced

degeneracies, an accidental $\mathcal{M}_{[001]}$ -protected nodal line (NL4) exists between bands 5 and 6 [Fig. 4(a) (left inset) and Fig. 4(b)]. As stabilized by the mirror $\mathcal{M}_{[001]}$, each line node in NL1-4 is shown to carry a zero-dimensional topological charge $Q = 1^{23}$, confirming the nontrivial topology of above nodal lines.

Along with the line degeneracies, Fig. 4(a)-(b) reveal two sets of Dirac points on the rotation/screw axes A - Γ and K - H , denoted as DP1 and DP2, with the stability guaranteed by the sixfold screw $\tilde{\mathcal{C}}_{6[001]}$ and threefold rotation $\mathcal{C}_{3[001]}$, respectively. If 2% compression along the b axis breaks $\mathcal{C}_{3[001]}$ and consequently opens up DP2, the crossing bands (bands 4 and 5) will become fully gapped, leading to a $\mathbb{Z}_2 = 1$. See Supporting Information for details. Therefore, topological surface states will emerge between bands 4 and 5³, as discussed below.

By constructing a semi-infinite (001) slab with the Pb termination, we demonstrate the momentum-resolved surface density of states (DOS) of $\text{Pb}_{1/3}\text{TaS}_2$ in Fig. 4(c). High-symmetry points in the reduced surface BZ are given in Fig. 4(b). Surface states and the corresponding bulk line or point nodes are labeled. Along the \bar{M} - $\bar{\Gamma}$ - \bar{M} path [left panel of Fig. 4(c)], surface states related to DP1, DP2 and NL3 are observed in turn from low to high energy. The surface band SS'2 is particularly illustrated in the left zoom-in view of Fig. 4(c). SS'2 consistently appears even if DP2 is opened up by a symmetry breaking (e.g., compression along the b axis), because of the inverted band structure and the resulting \mathbb{Z}_2 invariant 1. Along the \bar{K} - \bar{X}_1 - \bar{K} direction [right panel of Fig. 4(c)], line nodes responsible for NL1, NL2 and NL3, as well as the induced boundary modes are emergent. We note that NL4 is covered by the high-intensity surface modes from NL3, therefore invisible in the surface spectrum.

Discussions

Although many candidates of NLSMs have been proposed, experimental realizations of NLSMs are still relatively scarce^{17,49}. One of the biggest challenges is that the most of the NLSMs theoretically predicted are fragile to SOC (e.g., PbTaS_2 ³² and SnTaS_2 ³³). In our study, we have proposed a new TCM $\text{Pb}_{1/3}\text{TaS}_2$ hosting nodal-line structures, which remain stable even under significant SOC by virtue of the nonsymmorphic symmetry protection, and hence can be observed in a realistic experiment. Remarkably, $\text{Pb}_{1/3}\text{TaS}_2$ also possesses multiple Dirac points that can be driven into a TI phase by breaking the rotation symmetry. We predict Dirac-cone-like surface modes on the (001) surface, owing to the nontrivial band topology. Moreover, the q-2D feature and anisotropic transport are also supported by the band dispersions. Our results signify that $\text{Pb}_{1/3}\text{TaS}_2$ could act as a prospective platform to study the interaction between topological property and superconductivity. For the future work, angle-resolved photoemission spectroscopy (ARPES) and scanning tunneling microscopy (STM) studies are needed to identify the band structure

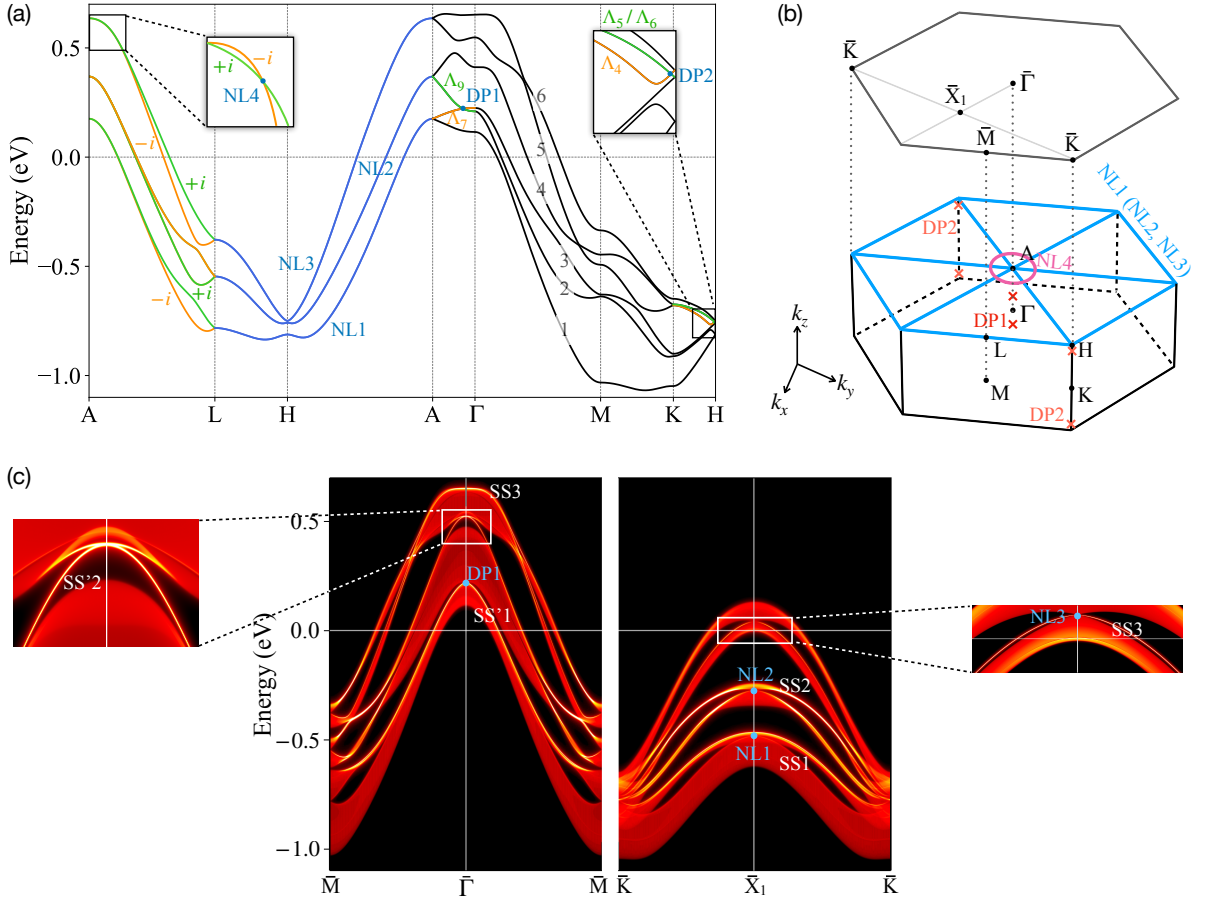


FIG. 4. Electronic structure of Pb_{1/3}TaS₂. (a) Electronic bands along a high-symmetry path. Energy is measured from the Fermi level. Orange and green distinguish crossing bands with different symmetry operation eigenvalues or irreducible representations (IRs). Dirac line and point degeneracies are labeled and highlighted in blue. Note that along the Γ -M-K-H line, all the seemingly gap closings are actually open at the meV scale except for DP2 and those at point H. Insets display zoom-in views of the band structure. The band gap in the left inset is exaggerated to enhance the visibility. (b) Brillouin zone (BZ) and surface BZ of Pb_{1/3}TaS₂. High-symmetry points are marked. Dirac nodal lines and points are indicated. (c) Momentum-resolved densities of states (DOS) of a semi-infinite (001) Pb-terminated slab. Yellow and dark red correspond to high and low density, respectively. The bulk nodes as well as surface states are highlighted.

and superconducting gap directly.

In summary, from first-principles calculations, the centrosymmetric Pb_{1/3}TaS₂ manifests multiple nodal states along with Dirac-cone-like surface states in the presence of SOC. Additionally, our experimental results suggest q-2D superconductivity with highly anisotropic features in this system. The combination of nontrivial band topology and superconductivity makes Pb_{1/3}TaS₂ a new candidate for further research of TSCs. Our work presents an important breakthrough in searching for new topological phases by building blocks design based on symmetry analysis.

Methods

Sample preparation The Pb_{1/3}TaS₂ single crystals were prepared by the chemical vapor transport (CVT) method. Stoichiometric amounts of high-purity Pb, Ta, S powders with the transport agents PbBr₂ (10 mg/cm³

in concentration) were thoroughly mixed and sealed in an evacuated quartz tube. The tube was heated at 1173 K with a temperature gradient of 5 K/cm for one week in a two-zone furnace.

Measurements The X-ray diffraction (XRD) pattern was performed on a Bruker D8 Advance X-ray diffractometer with Cu-K_α radiation. The chemical composition was determined by an energy-dispersive x-ray (EDX) spectrometer (Model Octane Plus) affiliated to a Zeiss Gemini 450 Schottky field emission scanning electron microscope (SEM). The transport measurements were measured on an Oxford superconducting magnet system equipped with a ³He cryostat. The DC magnetization was carried out on a Quantum Design magnetic property measurement system (MPMS3).

Band calculations The density functional theory (DFT) calculations are performed using the Vienna *ab*

initio simulation package (VASP)⁵⁰, based on the generalized gradient approximation (GGA) method under the Perdew-Burke-Ernzerhoff (PBE) parameterization⁵¹. The energy cutoff of the plane wave is 323.4 eV. The Brillouin zone (BZ) is sampled by a $12 \times 12 \times 4$ grid for the self-consistent calculations. Irreducible representations (IRs) of electronic eigenstates at high-symmetry k -points are determined via an in-house code and the software package *irvsp*⁵². Wannier functions are constructed by projecting Bloch states onto Ta $5d$ orbitals through WANNIER90^{53–55} without the iterative maximal localization procedure. Nodal lines or points and surface spectrum are computed with the WANNIERTOOLS package⁵⁶, where the latter is based on the iterative Green's function method⁵⁷. Pre/Post-processing tools and utilities for solids computation^{58–61} are exploited.

Data availability

The data that support the findings of this study are available from the corresponding author upon reasonable request.

Acknowledgments

The authors are grateful to Chao Cao, Wei Zhu and Takuya Nomoto for helpful discussion. C.X. acknowledges the computational resources at the HPC center at Hangzhou Normal University in China and the

RIKEN Center in Japan. This research was supported by the National Natural Science Foundation of China via Project 11904294 and 11774305, National Key Projects for Research & Development of China (Grant No. 2019YFA0308602), Zhejiang Provincial Natural Science Foundation of China under Grant No. LQ19A040005 and the foundation of Westlake Multidisciplinary Research Initiative Center (MRIC)(Grant No. MRIC20200402). M.H. acknowledges the support from JST CREST (Grants No. JPMJCR19T2). The authors thank the support provided by Dr. Xiaohe Miao and Dr. Lin Liu from Instrumentation and Service Center for Physical Sciences at Westlake University.

Author contributions

X.Y. conceived the project and grew the $\text{Pb}_{1/3}\text{TaS}_2$ single crystals, X.Y. performed the characterization and analyzed the data with the help of J.W., W.H., Z.X., T.W. and C.Z.. T.Y. and C.X. performed the first-principles calculations and analyzed the electronic structure. X.Y., T.Y. and X.L. wrote the manuscript with contributions from all authors.

Additional information

Competing interests: The authors declare no competing interests.

-
- [1] Chen, Y. L. *et al.* Experimental realization of a three-dimensional topological insulator, Bi_2Te_3 . *Science* **325**, 178–181 (2009).
 - [2] Moore, J. E. The birth of topological insulators. *Nature* **464**, 194–198 (2010).
 - [3] Hasan, M. Z. & Kane, C. L. Colloquium: topological insulators. *Rev. Mod. Phys.* **82**, 3045–3067 (2010).
 - [4] Ando, Y. Topological insulator materials. *J. Phys. Soc. Jpn.* **82**, 102001 (2013).
 - [5] Liu, Z. K. *et al.* Discovery of a three-dimensional topological dirac semimetal, Na_3Bi . *Science* **343**, 864–867 (2014).
 - [6] Lv, B. Q. *et al.* Experimental discovery of weyl semimetal TaAs. *Phys. Rev. X* **5**, 031013 (2015).
 - [7] Borisenko, S. *et al.* Time-reversal symmetry breaking type-ii weyl state in YbMnBi_2 . *Nat. commun.* **10**, 3424 (2019).
 - [8] Bian, G. *et al.* Topological nodal-line fermions in spin-orbit metal PbTaSe_2 . *Nat. Commun.* **7**, 10556 (2016).
 - [9] Neupane, M. *et al.* Observation of topological nodal fermion semimetal phase in ZrSiS . *Phys. Rev. B* **93**, 201104 (2016).
 - [10] Wan, X., Turner, A. M., Vishwanath, A. & Savrasov, S. Y. Topological semimetal and fermi-arc surface states in the electronic structure of pyrochlore iridates. *Phys. Rev. B* **83**, 205101 (2011).
 - [11] Wang, Z. *et al.* Dirac semimetal and topological phase transitions in A_3Bi ($A = \text{Na}, \text{K}, \text{Rb}$). *Phys. Rev. B* **85**, 195320 (2012).
 - [12] Burkov, A. A., Hook, M. D. & Balents, L. Topological nodal semimetals. *Phys. Rev. B* **84**, 235126 (2011).
 - [13] Young, S. M. *et al.* Dirac semimetal in three dimensions. *Phys. Rev. Lett.* **108**, 140405 (2012).
 - [14] Burkov, A. Topological semimetals. *Nat. Mater.* **15**, 1145–1148 (2016).
 - [15] Hirayama, M., Okugawa, R., Miyake, T. & Murakami, S. Topological dirac nodal lines and surface charges in fcc alkaline earth metals. *Nat. commun.* **8**, 14022 (2017).
 - [16] Hirayama, M., Okugawa, R. & Murakami, S. Topological semimetals studied by Ab initio calculations. *J. Phys. Soc. Jpn.* **87**, 041002 (2018).
 - [17] Fujioka, J. *et al.* Strong-correlation induced high-mobility electrons in dirac semimetal of perovskite oxide. *Nat. commun.* **10**, 362 (2019).
 - [18] Yamada, R. *et al.* Large variation of dirac semimetal state in perovskite CaIrO_3 with pressure-tuning of electron correlation. *Phys. Rev. Lett.* **123**, 216601 (2019).
 - [19] Molina, R. A. & González, J. Surface and 3d quantum hall effects from engineering of exceptional points in nodal-line semimetals. *Phys. Rev. Lett.* **120**, 146601 (2018).
 - [20] Kopnin, N. B., Heikkilä, T. T. & Volovik, G. E. High-temperature surface superconductivity in topological flat-band systems. *Phys. Rev. B* **83**, 220503 (2011).
 - [21] Young, S. M. & Kane, C. L. Dirac semimetals in two dimensions. *Phys. Rev. Lett.* **115**, 126803 (2015).
 - [22] Fang, C., Chen, Y., Kee, H.-Y. & Fu, L. Topological nodal line semimetals with and without spin-orbital coupling. *Phys. Rev. B* **92**, 081201 (2015).
 - [23] Yang, B.-J., Bojesen, T. A., Morimoto, T. & Furusaki,

- A. Topological semimetals protected by off-centered symmetries in nonsymmorphic crystals. *Phys. Rev. B* **95**, 075135 (2017).
- [24] Li, S. *et al.* Nonsymmorphic-symmetry-protected hourglass dirac loop, nodal line, and dirac point in bulk and monolayer $X_3\text{SiTe}_6$ ($X = \text{Ta}, \text{Nb}$). *Phys. Rev. B* **97**, 045131 (2018).
- [25] Chen, Y., Lu, Y.-M. & Kee, H.-Y. Topological crystalline metal in orthorhombic perovskite iridates. *Nat. commun.* **6**, 6593 (2015).
- [26] Chen, P.-J., Chang, T.-R. & Jeng, H.-T. Ab initio study of the PbTaSe_2 -related superconducting topological metals. *Phys. Rev. B* **94**, 165148 (2016).
- [27] Bian, G. *et al.* Drumhead surface states and topological nodal-line fermions in TiTaSe_2 . *Phys. Rev. B* **93**, 121113 (2016).
- [28] Li, Y. *et al.* Anisotropic gapping of topological weyl rings in the charge-density-wave superconductor In_xTaSe_2 . *Sci. Bull.* **66**, 243–249 (2021).
- [29] Li, Y. *et al.* Enhanced anisotropic superconductivity in the topological nodal-line semimetal In_xTaS_2 . *Phys. Rev. B* **102**, 224503 (2020).
- [30] Du, Y. *et al.* Emergence of topological nodal lines and type-II weyl nodes in the strong spin-orbit coupling system InNbX_2 ($X = \text{S}, \text{Se}$). *Phys. Rev. B* **96**, 235152 (2017).
- [31] Guan, S. Y. *et al.* Superconducting topological surface states in the noncentrosymmetric bulk superconductor PbTaSe_2 . *Sci. Adv.* **2**, e1600894 (2016).
- [32] Gao, J. J. *et al.* Superconducting and topological properties in centrosymmetric PbTaS_2 single crystals. *J. Phys. Chem. C* **124**, 6349–6355 (2020).
- [33] Chen, D.-Y. *et al.* Superconducting properties in a candidate topological nodal line semimetal SnTaS_2 with a centrosymmetric crystal structure. *Phys. Rev. B* **100**, 064516 (2019).
- [34] Fang, C. M., Wiegiers, G. A., Meetsma, A., De Groot, R. A. & Haas, C. Crystal structure and band structure calculations of $\text{Pb}_{1/3}\text{TaS}_2$ and $\text{Sn}_{1/3}\text{NbS}_2$. *Physica B* **226**, 259–267 (1996).
- [35] Katzke, H., Tolédano, P. & Depmeier, W. Phase transitions between polytypes and intralayer superstructures in transition metal dichalcogenides. *Phys. Rev. B* **69**, 134111 (2004).
- [36] Nagata, S. *et al.* Superconductivity in the layered compound 2H-TaS_2 . *J. Phys. Chem. Solids* **53**, 1259 – 1263 (1992).
- [37] Ali, M. N., Gibson, Q. D., Klimczuk, T. & Cava, R. J. Noncentrosymmetric superconductor with a bulk three-dimensional dirac cone gapped by strong spin-orbit coupling. *Phys. Rev. B* **89**, 020505 (2014).
- [38] Micnas, R., Ranninger, J. & Robaszkiewicz, S. Superconductivity in narrow-band systems with local nonretarded attractive interactions. *Rev. Mod. Phys.* **62**, 113–171 (1990).
- [39] Iavarone, M. *et al.* Two-band superconductivity in MgB_2 . *Phys. Rev. Lett.* **89**, 187002 (2002).
- [40] Gurevich, A. Limits of the upper critical field in dirty two-gap superconductors. *Physica C* **456**, 160–169 (2007).
- [41] Majumdar, A. *et al.* Interplay of charge density wave and multiband superconductivity in layered quasi-two-dimensional materials: The case of 2H-NbS_2 and 2H-NbSe_2 . *Phys. Rev. Mater.* **4**, 084005 (2020).
- [42] Xing, X. *et al.* Two-band and pauli-limiting effects on the upper critical field of 112-type iron pnictide superconductors. *Sci. Rep.* **7**, 45943 (2017).
- [43] Lee, H.-S. *et al.* Effects of two gaps and paramagnetic pair breaking on the upper critical field of $\text{SmFeAsO}_{0.85}$ and $\text{SmFeAsO}_{0.8}\text{F}_{0.2}$ single crystals. *Phys. Rev. B* **80**, 144512 (2009).
- [44] Kano, M. *et al.* Anisotropy of the upper critical field in a Co-doped BaFe_2As_2 single crystal. *J. Phys. Soc. Jpn* **78**, 084719 (2009).
- [45] Gurevich, A. Enhancement of the upper critical field by nonmagnetic impurities in dirty two-gap superconductors. *Phys. Rev. B* **67**, 184515 (2003).
- [46] Morris, R. C. & Coleman, R. V. Anisotropic superconductivity in layer compounds. *Phys. Rev. B* **7**, 991–1001 (1973).
- [47] Eppinga, R. & Wiegiers, G. A. A generalized scheme for niobium and tantalum dichalcogenides intercalated with post-transition elements. *Physica B* **99B**, 121–127 (1980).
- [48] Carbotte, J. P. Properties of boson-exchange superconductors. *Rev. Mod. Phys.* **62**, 1027–1157 (1990).
- [49] Chen, C. *et al.* Dirac line nodes and effect of spin-orbit coupling in the nonsymmorphic critical semimetals $m\text{SiS}$ ($m = \text{Hf}, \text{Zr}$). *Phys. Rev. B* **95**, 125126 (2017).
- [50] Kresse, G. & Furthmüller, J. Efficient iterative schemes for ab initio total-energy calculations using a plane-wave basis set. *Phys. Rev. B* **54**, 11169–11186 (1996).
- [51] Perdew, J. P., Burke, K. & Ernzerhof, M. Generalized gradient approximation made simple. *Phys. Rev. Lett.* **77**, 3865–3868 (1996).
- [52] Gao, J., Wu, Q., Persson, C. & Wang, Z. Irvsp: to obtain irreducible representations of electronic states in the vasp. *Comp. Phys. Commun.* **261**, 107760 (2021).
- [53] Marzari, N. & Vanderbilt, D. Maximally localized generalized wannier functions for composite energy bands. *Phys. Rev. B* **56**, 12847–12865 (1997).
- [54] Souza, I., Marzari, N. & Vanderbilt, D. Maximally localized wannier functions for entangled energy bands. *Phys. Rev. B* **65**, 035109 (2001).
- [55] Pizzi, G. *et al.* Wannier90 as a community code: new features and applications. *J. Phys.: Condens. Matter* **32**, 165902 (2020).
- [56] Wu, Q., Zhang, S., Song, H.-F., Troyer, M. & Soluyanov, A. A. Wanniertools: An open-source software package for novel topological materials. *Comput. Phys. Commun.* **224**, 405 – 416 (2018).
- [57] Sancho, M. P. L., Sancho, J. M. L., Sancho, J. M. L. & Rubio, J. Highly convergent schemes for the calculation of bulk and surface green functions. *J. Phys. F: Met. Phys.* **15**, 851–858 (1985).
- [58] Wang, V., Xu, N., Liu, J., Tang, G. & Geng, W. Vaspkit: A user-friendly interface facilitating high-throughput computing and analysis using vasp code. *arXiv preprint arXiv:1908.08269* (2019).
- [59] Momma, K. & Izumi, F. Vesta: a three-dimensional visualization system for electronic and structural analysis. *J. Appl. Cryst.* **41**, 653–658 (2008).
- [60] Setyawan, W. & Curtarolo, S. High-throughput electronic band structure calculations: Challenges and tools. *Comp. Mater. Sci.* **49**, 299 – 312 (2010).
- [61] Togo, A. & Tanaka, I. Spglib: a software library for crystal symmetry search. *arXiv preprint arXiv:1808.01590* (2018).